Why are some galaxy clusters underluminous?

The very low concentration of the CL2015 mass profile

S. Andreon[1], A. Moretti[1], G. Trinchieri[1], and C. H. Ishwara-Chandra[2]

[1] INAF–Osservatorio Astronomico di Brera, Via Brera 28, 20121 Milano, Italy
e-mail: `stefano.andreon@brera.inaf.it`
[2] National Centre for Radio Astrophysics TIFR, P. B. No. 3., Ganeshkhind, 411007 Pune, India

ABSTRACT

Our knowledge of the variety of galaxy clusters has been increasing in the last few years thanks to our progress in understanding the severity of selection effects on samples. To understand the reason for the observed variety, we study CL2015, a cluster ($\log M_{500}/M_{\odot} = 14.39$) easily missed in X-ray selected observational samples. Its core-excised X-ray luminosity is low for its mass M_{500}, well below the mean relation for an X-ray selected sample, but only $\sim 1.5\sigma$ below that derived for an X-ray unbiased sample. We derived thermodynamic profiles and hydrostatic masses with the acquired deep *Swift* X-ray data, and we used archival *Einstein*, *Planck*, and Sloan Digital Sky Survey data to derive additional measurements, such as integrated Compton parameter, total mass, and stellar mass. The pressure and the electron density profiles of CL2015 are systematically outside the $\pm 2\sigma$ range of the universal profiles; in particular the electron density profile is even lower than the one derived from *Planck*-selected clusters. CL2015 also turns out to be fairly different in the X-ray luminosity vs. integrated pressure scaling compared to an X-ray selected sample, but it is a normal object in terms of stellar mass fraction. CL2015's hydrostatic mass profile, by itself or when is considered together with dynamical masses, shows that the cluster has an unusual low concentration and an unusual sparsity compared to clusters in X-ray selected samples. The different behavior of CL2015 is caused by its low concentration. When concentration differences are accounted for, the properties of CL2015 become consistent with comparison samples. CL2015 is perhaps the first known cluster with a remarkably low mass concentration for which high quality X-ray data exist. Objects similar to CL2015 fail to enter observational X-ray selected samples because of their low X-ray luminosity relative to their mass. The different radial dependence of various observables is a promising way to collect other examples of low concentration clusters.

Key words. galaxies: clusters: general – galaxies: clusters: intracluster medium – dark matter – X-rays: galaxies: clusters – radio continuum: galaxies – galaxies: clusters: individual: CL2015

1. Introduction

Galaxy clusters appear to obey tight scaling relations (e.g., Vikhlinin et al. 2006; Pratt et al. 2009) and to possess universal thermodynamic radial profiles (e.g., Arnaud et al. 2010; Sun et al. 2011; Ghirardini et al. 2019). Thermodynamic radial profiles (electron density, temperature, pressure, and entropy) offer a unique asset to the study of the properties of the intracluster medium, the dynamical status of the cluster, cluster formation and evolution, gas cooling, cluster energetics, and structure growth, all of which have prompted a large number of articles on these subjects.

It is now recognized that the X-ray selection deeply affects both scaling relations and quantities hinged on them, for example the cosmological parameter estimates: at a given mass, brighter-than-average clusters are easier to select and make part of a sample, while fainter-than-average clusters are easily missed (Stanek et al. 2006). Pacaud et al. (2007) show that the evolution of the $L_X - T$ scaling of an X-ray selected sample would be biased if selection effects were neglected, while Vikhlinin et al. (2009) accounted for the X-ray selection in their cosmological analysis, but making assumptions on the unseen population. Assumptions on the unseen (or poorly represented) cluster population are also adopted in scaling relation analyses, for example those of Pacaud et al. (2007), Maughan et al. (2012), Andreon & Hurn (2013),

and Mantz et al. (2016). Assumptions on the unseen population are also needed for samples that are complete in some observables, for example, that of Giles et al. (2017).

The risk associated with making assumptions on an unseen population has triggered a number of observational programs targeting, or also including, clusters more easily missed. Andreon & Moretti (2011) exploited the low and stable X-ray background of X-ray Telescope (XRT) on *Swift* for follow-ups of a sample of clusters free from the X-ray bias, finding a larger scatter in X-ray luminosity at a given richness than in X-ray selected samples (accounting for Malmquist and selection effect corrections for the latter). Several of these clusters have low surface brightness, which impair their detection in X-ray surveys. A similar effort was repeated by Ge et al. (2019) and by Pearson et al. (2017), the latter using *Chandra* data on groups and optical luminosity in place of richness, finding an increased scatter. Giles et al. (2015) followed up in X-ray a small sample of weak-lensing selected clusters. Andreon et al. (2009) and Andreon & Moretti (2011) observed the two most distant clusters free from the X-ray selection bias to constrain the evolution of the $L_X - T$ scaling without making a hypothesis on the unseen population. Because of the heavy censoring of X-ray selected samples, constraints derived from 100 X-ray selected clusters (Giles et al. 2016) are comparable with the one derived for just the two high redshift clusters above. In parallel, clusters selected by their

Sunayev–Zeldovich (SZ) signal turned out to also show a larger scatter than in X-ray selected samples (Planck Collaboration IX 2011, 2012), with some unexpected outlier clusters with a low X-ray luminosity for their SZ signal (Planck Collaboration XXVII 2016). These and other efforts led to the discovery of a growing variety of cluster properties at a given mass: X-ray luminosity and gas fraction have a larger scatter than previously thought (e.g., Andreon & Moretti 2011; Planck Collaboration IX 2011, 2012; Andreon et al. 2016, 2017; Giles et al. 2017; Rossetti et al. 2017), and clusters with low electron density profiles (Andreon et al. 2016), or of low surface brightness (Andreon et al. 2016; Xu et al. 2018) have been discovered.

It is plausible that X-ray selection effects have consequences on the measured mean thermodynamic radial profiles and their scatter. If brighter-than-average clusters are over-represented in X-ray samples, then the average electron density profile is expected to be biased toward the high end because $L_X \propto n_e^2$. The scatter is expected to be biased toward the low end because a reduced part of the whole population is in the sample (fainter-than-average clusters are under-represented when not missing altogether). The effect of X-ray selection on the other thermodynamic profiles is harder to predict, and should be taken from an observational perspective. However, obtaining high quality X-ray data for objects missing because they are intrinsically X-ray faint or of low surface brightness (for their mass) is observationally hard. This adds to the difficulty of having accurate masses for a sizeable sample, which is needed to identify outliers at a given mass.

This situation has been partially rectified by the first X-ray unbiased survey of clusters (XUCS; Andreon et al. 2016) because these clusters have high quality mass estimates. The sample consists of a velocity-dispersion-selected sample of clusters in the very nearby Universe and it is X-ray unbiased at a given mass, because the probability of inclusion of the cluster in the sample does not depend on its X-ray luminosity (or count rate) at a fixed mass. This property allowed a robust estimate of the scatter (see also Andreon et al. 2017), with a wider range in X-ray luminosity (both total and core excised) at a given mass than seen in the Representative X-ray selected sample (REXCESS; Pratt et al. 2009, after Malmquist- and selection-bias corrections) and in the *Planck*-selected clusters (Andreon et al. 2016). Similar conclusions are also proposed by Giles et al. (2017), making assumptions on the extent and size of the unseen population.

The XUCS sample also shows a larger scatter in gas fraction (Andreon et al. 2017). While accurate masses and well-determined X-ray luminosities of XUCS clusters are available, detailed investigation of the X-ray properties of these clusters that are gas poor or X-ray faint for their mass requires deeper observations than available. In this work, we present the deep X-ray follow-up of CL2015, selected because it has a low X-ray luminosity for its mass.

Throughout this paper, we assume $\Omega_M = 0.3$, $\Omega_\Lambda = 0.7$, and $H_0 = 70 \, \text{km} \, \text{s}^{-1} \, \text{Mpc}^{-1}$. Results of stochastic computations are given in the form $x \pm y$, where x and y are the posterior mean and standard deviation. The latter also corresponds to 68% intervals because we only summarize posteriors close to Gaussian in this way. All logarithms are in base 10.

2. Data analyis

2.1. Selection of CL2015

CL2015, also known as Abell 117 and PSZ2 G126.72−72.82, is an intermediate mass cluster ($\log M_{500}/M_\odot = 14.39 \pm 0.09$)
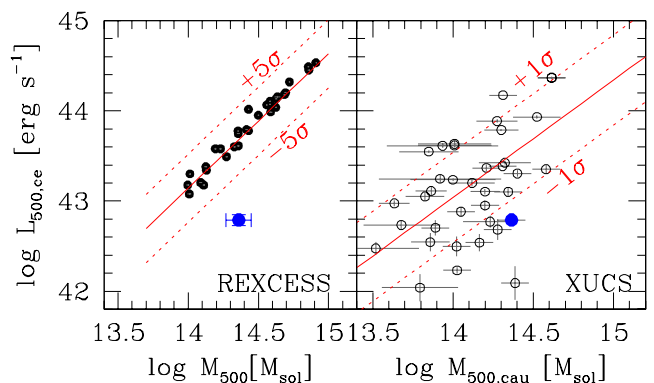

Fig. 1. Core-excised [0.5–2] keV band X-ray luminosity vs. mass M_{500}. *Left panel*: black points are REXCESS (X-ray selected) clusters and use Y_X-based masses. The red line is the Malmquist- and selection-bias-corrected fit to the REXCESS X-ray selected sample, whereas the dashed lines mark the mean relation $\pm 5\sigma_{intr}$. The blue outlying point is CL2015. *Right panel*: open circles are XUCS clusters, the blue point is CL2015. The red line and the $\pm 1\sigma$ corridor is a fit to this sample (Andreon et al. 2017).

in the nearby Universe ($z = 0.055$) with a core-excised X-ray luminosity of $\log L_{X,500,ce} = 42.79 \pm 0.06 \, \text{erg} \, \text{s}^{-1}$ ([0.5,2] keV band). This luminosity is entirely consistent with that reported by Jones & Forman (1999) based on the *Einstein* Imaging Proportional Counter data, within an angular aperture close to our $r_{500,cau}$, revised for cosmology, temperature ($T = 3$ keV, see Sects. 3.1 and 3.2), and energy band used here ($\log L_X = 42.99 \pm 0.03$ vs. $42.97 \pm 0.05 \, \text{erg} \, \text{s}^{-1}$ [0.5,2] keV band). The cluster has a richness of 0 in the Abell (1958) catalog.

The CL2015 core-excised luminosity is eight times fainter than expected based on its M_{500}, or about 12σ below the fit derived using the X-ray selected sample REXCESS (Pratt et al. 2009) after corrections applied to account for Malmquist and selection biases (see left panel of Fig. 1). In the analysis of XUCS, Andreon et al. (2009) remarked that the sample displays a larger scatter in X-ray luminosity at a given mass, relative to REXCESS (or other cluster samples analyzed before). In this sample, CL2015 is not as extreme, since it is located just ~1.5σ away from the average (right panel of Fig. 1) and has a ~1.5σ lower gas fraction than average Andreon et al. (2017).

This result does not depend on how the total mass is derived. There are three estimates of the mass within $\Delta = 500$, all consistent with each other: from the dynamical analysis of Abdullah et al. (2018), $\log M_{500,dyn} = 14.27$ (no error quoted), from the caustic technic, $\log M_{500,cau} = 14.36 \pm 0.09$, and from velocity dispersions calibrated with simulations, $\log M_{500,\sigma_v} = 14.27 \pm 0.12$ (Andreon et al. 2016). Details are given in Appendix A and we refer the reader to the original articles for more information on the technics used.

CL2015 is one of the many clusters ~1.5σ below the mean XUCS relation and has been chosen to minimize exposure time, leading us to select one of the nearest clusters in XUCS and one of the only two clusters, out of a sample of 34, with r_{500} slightly larger than the *Swift* field of view.

2.2. X-ray data reduction

We have re-observed CL2015 with XRT on board the *Swift* satellite for a total of 67 ks. We chose *Swift* because its low and stable background (Moretti et al. 2009) makes it the best choice for sampling a cluster expected to have low surface brightness

([Andreon & Moretti 2011](#)). Indeed, XRT is 1.5 times more sensitive than X-ray Multi-Mirror Mission (*XMM-Newton*) to low surface brightness emission ([Mushotzky et al. 2019](#); [Walker et al. 2019](#)) for the same exposure time.

For the *Swift* XRT data reduction and analysis we followed the procedures described in [Moretti et al. (2009)](#) for extended sources, with the following improvements. First of all, we were able to recover a section of the field of view previously discarded because it was contaminated by calibration radioactive sources onboard *Swift* that are significantly decayed by now. This allows us to recover ∼23% of the area in the single visit image, and up to ∼60% when images with different orientations are combined together. Second, measurements of extended sources of low intensity contaminated by a background require an accurate knowledge of the background itself. Due to the low telescope orbit, the *Swift* background is lower and more stable than *XMM-Newton* or *Chandra*; nevertheless, it displays very short periods of enhanced intensity and/or a spatial structure due to increased CCD temperature and bright Earth light reflection. In order to filter out the former, we applied a stricter filter to CCD temperature, $T < 55\,°C$. To eliminate low energy flares (due to the bright Earth light reflection), we extracted the light curve in the [0.3–0.5] keV band from the level 2 event file in CCD external regions (77 000 pixel in total) and filtered out time intervals where the count rate exceeded 5 c/s. Based on a more extensive XRT program led by us, we found that by flagging periods of enhanced intensity at these very low energies, the background is lowered by a factor of up to three at low energies, with a loss of less than 5–10% of the total exposure time.

The net observing time was 58 ks after cleaning the data from increased background periods. Since the field of view of the observation is entirely filled with the cluster emission, we also use four fields (at high latitude) centered on gamma ray bursts to account for background. We removed the first part of the exposure, contaminated by the gamma ray burst, and reduced the exposure time to resolve the background sources at similar levels in the cluster and control field directions. The final background exposures are 25, 37, 29, and 27 ks, which are lower than the cluster's because source detectability is easier in observations lacking a cluster diffuse emission.

Point sources are detected by a wavelet detection algorithm, and we masked pixels affected by them when calculating radial profiles and fluxes. In our analysis, we used energy-dependent exposure maps to calculate the effective exposure time, accounting for dithering, vignetting, CCD defects, gaps, and excised regions. Since *Swift* observations are taken with different roll angles that result in different exposures at different off-axis angles, we only consider regions where the exposure time is larger than 50% of the central value. To check the validity of our analysis relative to that of different authors, methods, and telescopes, we also applied the same procedure to Abell 2029, which was also observed by *Swift* for 34 ks and is in the XMM Cluster Outskirts Project (X-COP) sample ([Ghirardini et al. 2019](#)).

3. Results

3.1. Projected quantities

Figure [2](#) shows the [0.5–2] keV image and the region considered here, limited by the line defining where the exposure time is 50% of the central value (roughly a circle with a diameter of ∼22′). There are about 5400 net photons in the [0.3–7] keV band in the unflagged regions. The X-ray image lacks any strong evidence of bimodality or other irregularities, and the cluster looks
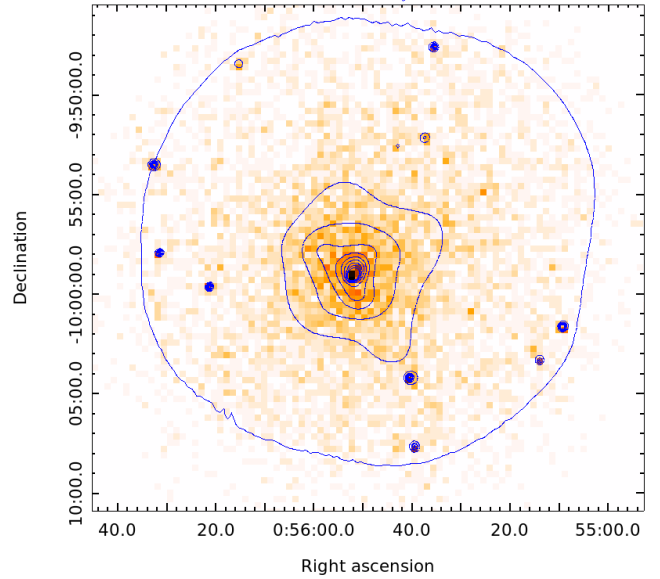

Fig. 2. X-ray contours from an adaptively smoothed image (with a minimum significance of 3σ) superimposed onto the binned image ([0.5–2] keV energy band). Contours are in steps of 0.2 counts per 5.53″ pixel, starting from 0.3. The outer region denotes the locus where exposure time is 50% of the on-axis exposure time.

radially symmetric. The cluster center is iteratively computed as the centroid of X-ray emission within the inner 20 kpc. It is 12 kpc north of the Brightest Cluster Galaxy (BCG) well within its optical size.

We derived spectra in four different annular regions, and we assumed an absorbed Astrophysical Plasma Emission Code (APEC) model ([Smith et al. 2001](#)), with free metal abundance fixed at solar ratios ([Anders & Grevesse 1989](#)). We fixed the absorbing column at the Galactic value and the redshift at cluster redshift. The fit accounts for variations in exposure, flagged regions, and background, the latter being measured in the same angular annuli but in our four background fields. The spectral counts were grouped to a minimum of five per bin and were fit with the XSPEC spectral package using the modified *C*-statistic (also called *W*-statistic in XSPEC), in analogy with [Willis et al. (2005)](#). Simulations in [Willis et al. (2005)](#) confirm that resampling the data to prevent the occurrence of spectral bins containing zero counts minimizes temperature biases and this approach is currently used by many authors.

Figure [3](#) shows the spectral distribution of the counts (3400 net photons in $0.3-7.0$ keV band) in the $0.15 < r/r_{500,\mathrm{cau}} < 0.5$ corona, compared with the best fit model, at $kT = 2.85 \pm 0.21$ keV and abundance 0.3 ± 0.1 solar. The line blend at $kT \sim 1$ keV is evident in the spectrum. We also extracted spectra in the radial ranges $0.0 < r/r_{500,\mathrm{cau}} < 0.15$, $0.15 < r/r_{500,\mathrm{cau}} < 0.25$, and $0.25 < r/r_{500,\mathrm{cau}} < 0.5$. Each annulus contains >1400 net photons. We found a fairly flat projected temperature profile, as shown by Fig. [4](#). Finally, we found no temperature differences among the four quadrants with $1' < r < 0.5r_{500,\mathrm{cau}}$.

We then measured the azimuthally-averaged surface brightness, which was corrected for exposure time, vignetting, and excluded regions, in the cluster and in the background fields. We measured the surface brightness in six energy bands ([$0.3-0.5$], [$0.5-1$], [$1-2$], [$2-3$], [$3-5$], and [$5-7$] keV) and in 21 annuli of increasing width to balance the decreasing signal-to-noise ratio with increasing radius. The smallest bin width allowed is 10″, comparable to the XRT point spread function (PSF). Since the
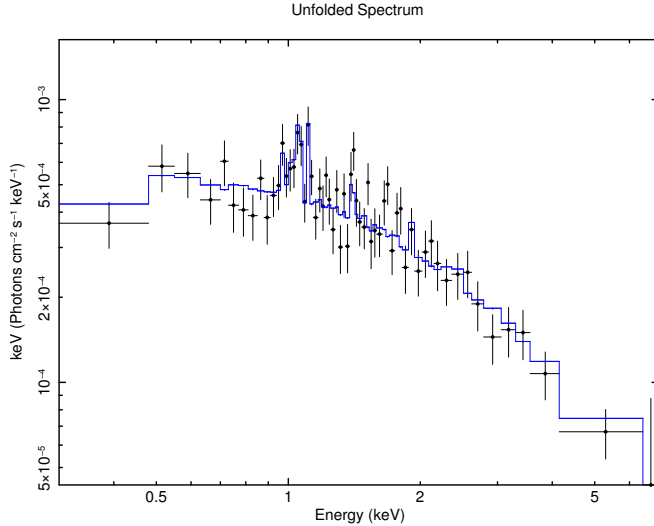
Unfolded Spectrum

Fig. 3. CL2015 X-ray spectrum in the $0.15 < r/r_{500,\text{cau}} < 0.5$ range and best fitting model. The spectrum is rebinned for display purposes, but is fitted on a minimally binned version.
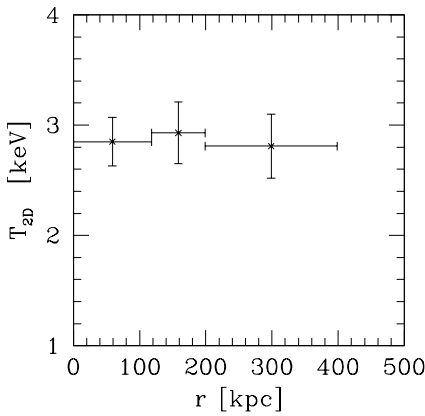

Fig. 4. CL2015 projected temperature profile.

radial profiles derived in the four background fields are consistent, we used the averaged profile.

Figure 5 shows the distribution of the total counts per unit area in different bands (points). We have on average 45 net photons per energy-radius bin.

3.2. Thermodynamic profiles

Thermodynamic profiles were derived using MBPROJ2 (Sanders et al. 2018), a Bayesian forward-modeling projection code that fits the surface brightness profiles (in different energy bins) accounting for the background. The forward modeling goes beyond the limitations of previous approaches, which were obliged to "paste" tailored-cut deconvolved and convolved profiles (e.g., Pratt & Arnaud 2005), apply arbitrary regularization kernels (e.g., Planck Collaboration III 2013) to deal with noise, or ignore temperature gradients when deriving the electron density profile for clusters showing large temperature gradients (e.g., XCOP, Ghirardini et al. 2019). As in other approaches, MBPROJ2 makes the usual assumptions about cluster sphericity, clumping, and, when requested, hydrostatic equilibrium.

We fit the data twice to understand the impact of assumptions on the derived thermodynamic profiles. In the first fit, a

descriptive analysis, we opted for an approach similar to Vikhlinin et al. (2006) and we modeled the temperature and electron density profiles with flexible functions constrained by the data. This is a fit aimed at simply describing the observations, with models introduced to impose regularity and smoothness. In particular, the MBPROJ2 code models the electron density as a modified single-β profile following Vikhlinin et al. (2006):

$$n_\text{e}^2 = n_0^2 \frac{(r/r_c)^{-\alpha}}{(1 + r^2/r_c^2)^{3\beta - \alpha/2}} \frac{1}{(1 + r^\gamma/r_\text{s}^\gamma)^{\epsilon/\gamma}}. \tag{1}$$

Similarly to Vikhlinin et al. (2006), the temperature profile is given by the product of a broken power law with three slopes and a term introduced to model the temperature decline in the core region:

$$T = T_0 \frac{((r/r_c')^{a_\text{cool}} + (T_\text{min}/T_0))}{(1 + (r/r_c')^{a_\text{cool}})} \frac{(r/r_\text{t})^{-a}}{(1 + (r/r_\text{t})^b)^{c/b}}. \tag{2}$$

The other thermodynamic profiles are derived from the ideal gas law. Following Vikhlinin et al. (2006), we fix $\gamma = 3$, and following Sanders et al. (2018) we use weak priors for the remaining six free electron density parameters. Following McDonald et al. (2014), we fix the inner slope to $a = 0$ and the shape parameter of the inner region to $a_\text{cool} = 2$.

In the second fit, we adopt instead a physical model for the cluster: we assume a Navarro et al. (1997; hereafter NFW) mass profile (for the dark matter only) and hydrostatic equilibrium, which makes explicit temperature profile modeling unnecessary. In this case, MBPROJ2 computes the pressure profile given the NFW mass profile and derives the other thermodynamic profiles combining it with the electron density profile. As in our descriptive analysis, parameters are determined by fitting the data.

In both fits, metallicity is a free parameter, absorption was fixed at the Galactic N_H value in the direction of the cluster from Kalberla et al. (2005), and the results are marginalized over a further background scaling parameter to account for systematics (differences in background level between the cluster and control fields). The model is integrated on the same energy and radial bins as the observations, so that the results do not depend on binning.

In practice, the electron density profile is robustly determined because it is the deprojected surface brightness profile (after a change of units with a minimal temperature dependence that is ignored in major observational programs such as X-COP and REXCESS). Temperature is measured from the ratio of the cluster brightness in different energy bands, and temperature gradients are derived from radial variations in these ratios. Radial temperature gradients are usually small, except in cool cores, to such a point that projected temperatures are often overplotted on deprojected temperatures (e.g., Vikhlinin et al. 2005; Sun et al. 2009), which makes deprojection robust provided the radial profiles are regularized (by assuming a smooth temperature or mass profile shape). The other profiles come from $P = n_\text{e}T$ and $K = T/n_\text{e}^{2/3}$.

As done in the literature, the three-dimensional thermodynamic profiles are derived from the one-dimensional profiles (cf. in Fig. 5) under several assumptions that include: (a) spherical symmetry, that is, concentric isodensities of identical center, position angle, and zero ellipticity; (b) smooth, unclumped gas distribution without any substructure; and (c) how and how much the observed radial profiles are regularized or the fitted model is constrained by assumptions. In particular, the errors computed (by us and others) depend on all these assumptions and, given that clusters are known to deviate somewhat from the
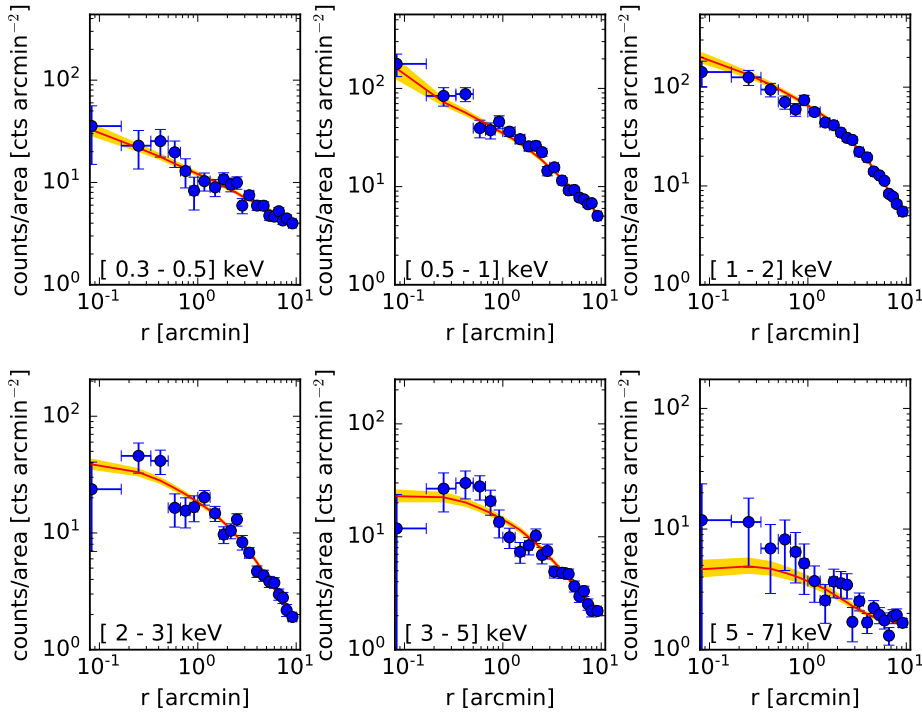
Fig. 5. CL2015 radial surface brightness profiles. Observed counts are indicated with points, whereas error bars mark $\sqrt{n}$ for display purposes only. The solid line is the mean fitted (physical) model (see Sect. 3.2) while the shading indicates the 68% uncertainty.

ideal assumed behavior, errors should always be regarded as an underestimate of the true uncertainty.

To test our ability to derive thermodynamic profiles against state-of-the-art analyses, we compared the thermodynamic and mass profiles of Abell 2029 derived by us using *Swift* with the same technique described here for CL2015 with those derived using *XMM-Newton* by Ghirardini et al. (2019). The profiles agree well with each other, as detailed in the Appendix.

CL2015 surface brightness profiles are well fitted in the various bands by our physical model (Fig. 5). This is also true for the descriptive model. Profiles extend to about r_{1000} (r_Δ values are derived in the next section), where the cluster contribution is still >5% of the background level. The model captures well the data trend, being almost always within (approximately) 1σ of the data. This is unsurprising given that we used flexible functions, with 11 or 14 free parameters, that act as regularization kernels, to model the data.

Figure 6 shows CL2015 thermodynamic profiles derived both in our descriptive analysis (solid line with error bars) and with the assumption of hydrostatic equilibrium and a NFW mass profile (solid line with shading). The descriptive and physical profiles, which are posterior distributions, turn out to be indistinguishable where the data (the likelihood) dominate, while they differ in the low signal-to-noise (S/N) regime, where the prior dominates, namely at the very center, for three out of the four thermodynamic quantities considered, as also discussed in Sanders et al. (2018) for a different sample. Differences at the center are due to the small volume within a sphere of small radius r, and to the presence of many photons emitted outside the sphere but inside the cylinder of radius r, which lowers the S/N of the central quantities. Since the signal coming from the central volume is noisy, the prior dominates. Instead, quantities measured outside the very center and global quantities, such as the mean or integrated value within r_{2500}, are not affected by these modeling differences. In summary, derived thermodynamic profiles are robust to (tested) assumptions, with the exception of the very center for strongly T-sensitive quantities. We tested that
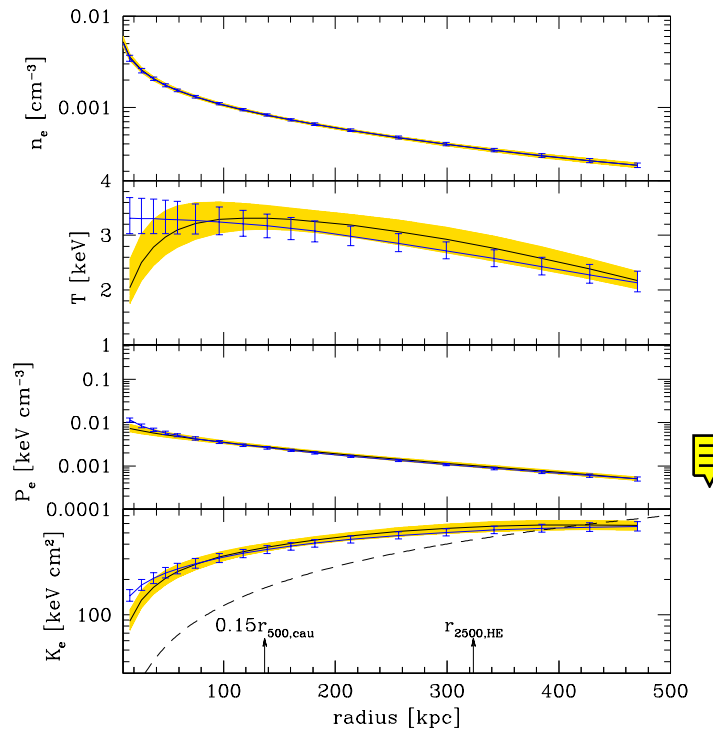

Fig. 6. CL2015 thermodynamic profiles. The solid line with shading shows our physical fit, while the solid line with error bar is our descriptive fit. In both cases we plot the mean model and 68% errors. The dashed curve in the entropy panel is the Voit et al. (2005) fit to non-radiative simulations, as adapted by Pratt et al. (2010).

the electron density profile derived here agrees with our previous determination (Andreon et al. 2017) from shallower *Swift* data, which required stronger assumptions.

We found $\log K_{2500} = 2.71 \pm 0.03 \, \text{keV cm}^{-2}$, $T_{2500} = 2.6 \pm 0.2 \, \text{keV}$, and $f_{\text{gas},2500} = 0.043 \pm 0.005$, almost indepedent of the
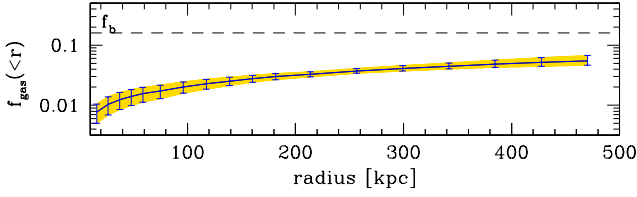
Fig. 7. CL2015 enclosed gas fraction profile from the physical modeling. The horizontal dashed line shows the Universe value.
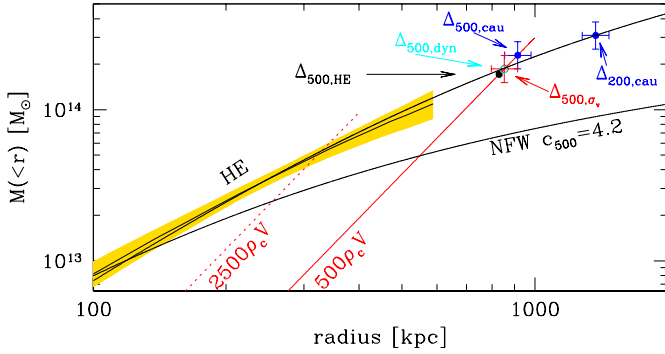

Fig. 8. CL2015 mass comparison. Hydrostatic mass (HE) within the radius r (black solid curve) is compared to $500\rho_c V$ (solid red line), $2500\rho_c V$ (dotted red line), and to caustic, velocity-dispersion-based, and other dynamical masses (blue, red, and cyan points, respectively). We also plot a NFW profile with $c_{500} = 4.2$ normalized at $r = 100\,$kpc (bottom curve) and NFW profile with $c_{500} = 1.5$ normalized at r_{200} (top curve fitting all data).

fitting model (see Fig. 6), and an abundance 0.23 ± 0.12 solar for both fits (the latter in agreement with the 2D analysis). Figure 6 shows that in CL2015 there is an entropy excess compared to the non-radiative simulations of Voit et al. (2005), as commonly found in clusters. Figure 7 shows the enclosed gas fraction profile derived with the physical fit.

3.3. Concentration of the cluster mass

Figure 8 plots the mass profile $M(<r)$ fitted to our X-ray data under the assumption of hydrostatic equilibrium. The intercept with $\Delta\rho_c V$ gives, by definition, $r_{\Delta,\mathrm{HE}}$ and $M_{\Delta,\mathrm{HE}}$, where the subscript "HE" emphasizes that we assume hydrostatic equilibrium. Our data reach $\Delta = 1000$. This is the same radius covered with the sample of clusters in Arnaud et al. (2005), which is used to calibrate the REXCESS (e.g., Pratt et al. 2009) and *Planck* (e.g., Planck Collaboration XXIX 2014) scaling relations. Values at overdensity $\Delta = 2500$ are well measured, with no extrapolation, and we find $\log M_{2500,\mathrm{HE}}/M_\odot = 13.69 \pm 0.09$ (and therefore $\log r_{2500,\mathrm{HE}} = 2.51 \pm 0.03$). Values at $\Delta = 500$ require some extrapolation, and we find $\log M_{500,\mathrm{HE}}/M_\odot = 14.23 \pm 0.22$ (and therefore $\log r_{500,\mathrm{HE}} = 2.92 \pm 0.08$). The extrapolation to $\Delta = 500$ is commonly done even for clusters with very high quality data, such as those used by Arnaud et al. (2005).

Figure 8 also shows the other estimates of mass of CL2015 at $\Delta = 500$, from the three dynamical analyses by two different teams (Sect. 2.1 and Appendix A). All four estimates of mass, of which one is hydrostatic and three are dynamical, agree with each other. No matter which M_{500} is taken, CL2015 remains an outlier, at $>5\sigma$, in the REXCESS $L_X - M_{500}$ relation.

Figure 8 also shows the estimate of caustic mass at the best constrained overdensity, $\Delta = 200$ ($M_{200} = 14.49 \pm 0.09$), and a NFW profile with $c_{500} = 4.2$, a typical value measured in
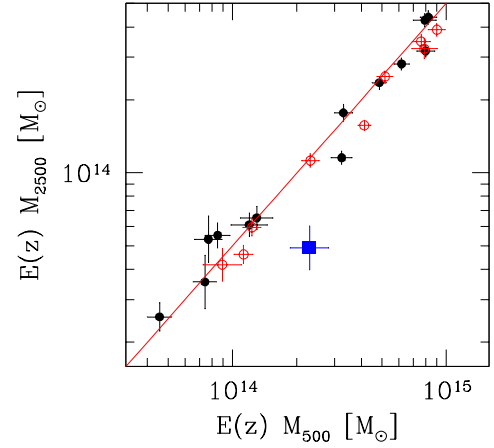

Fig. 9. Mass at different overdensities comparison. Masses at two different overdensities, $\Delta = 500$ and $\Delta = 2500$, of CL2015 (blue point), and clusters in Vikhlinin et al. (2006) and Sun et al. (2009) (solid points) and Arnaud et al. (2005, open points) are shown. The red line is the location $M_{500}/M_{2500} = 2.0$.
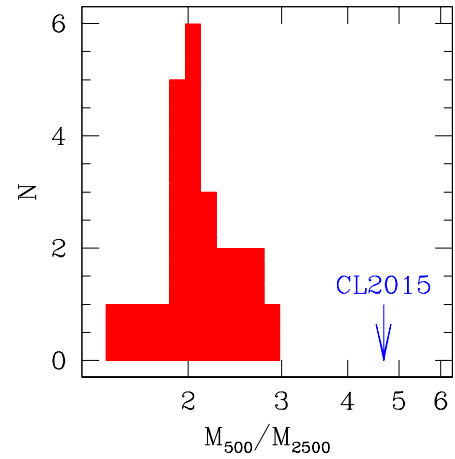

Fig. 10. Inverse sparsity comparison. The arrow marks the value of M_{500}/M_{2500} of CL2015 while the histogram shows the distribution of clusters in Vikhlinin et al. (2006), Sun et al. (2009), and Arnaud et al. (2005).

hydrostatic analyses (e.g., Vikhlinin et al. 2005; Sun et al. 2009), arbitrarily normalized at $r = 100\,$kpc. A NFW profile with such a high concentration, however, does not reproduce the mass distribution of CL2015: with the adopted normalization, there is a significant mass excess at large radii in CL2015, or deficit at small radii, relative to other clusters with $c_{500} \sim 4.2$. This is true also ignoring dynamical estimates of mass. A lower value of $c_{500} = 1.5 \pm 0.4$ instead fits all data (upper curve in Fig. 8).

Figure 9 reiterates the point: clusters with a given value of the ratio M_{500}/M_{2500} (inverse sparsity in Corasaniti et al. 2018), would be aligned on a line parallel to the one drawn, $M_{500}/M_{2500} = 2.0$, appropriate for a cluster of $c_{500} = 4.2$. This ratio is observed in the samples of (morphologically relaxed) clusters in Vikhlinin et al. (2006), Sun et al. (2009, closed points), and Arnaud et al. (2005, open points). In the figure, to filter out noisy measurements we only consider clusters with measured M_{500} with errors less than 0.1 dex and we removed clusters noted by the authors as having largely extrapolated r_{500} or values that should be treated with caution. CL2015 is a clear outlier in concentration, with $M_{500}/M_{2500} = 4.7$. Figure 10 reinforces this point: with $M_{500}/M_{2500} = 4.7$, CL2015 is extreme when
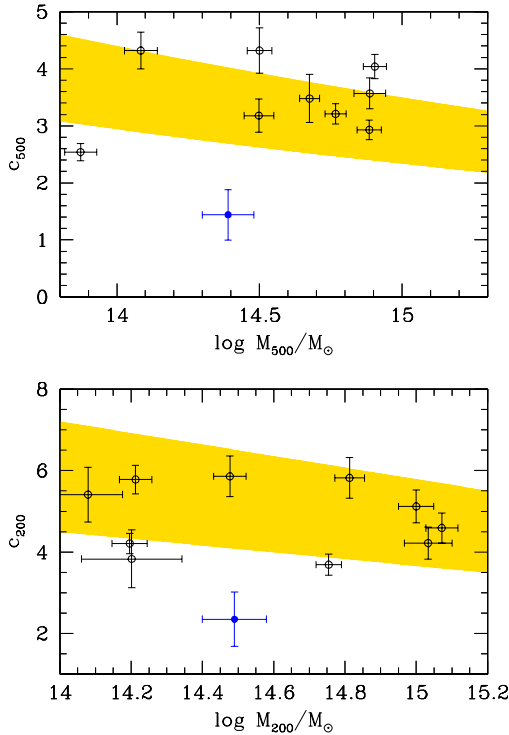
Fig. 11. Concentration comparison. *Top and bottom panels*: compare CL2015 to clusters in Vikhlinin et al. (2006) and to clusters in Pointecouteau et al. (2005). The shadings indicate $\pm 1\sigma$ scatter around the theoretical prediction by Dolag et al. (2004).

compared to values in the above cluster samples. Since we have centered the cluster on the X-ray peak (and the BCG), the observed low concentration does not come from having miscentered the cluster. CL2015 would still be an outlier in sparsity if we used its hydrostatic mass instead of caustic mass, which would give $M_{500}/M_{2500} = 3.8$.

From masses at $\Delta = 2500$ and $\Delta = 200$ we derived a concentration of $c_{200} = 2.4 \pm 0.7$ and $c_{500} = 1.5 \pm 0.4$. Figure 11 compares CL2015's concentration with determinations from Vikhlinin et al. (2006) and Pointecouteau et al. (2005), and theoretical predictions from Dolag et al. (2004). In the sample of Pointecouteau et al. (2005), all measurements are extrapolated to $\Delta = 200$, since, as mentioned, these reach $\Delta \sim 1000$ only. Also in these plots, CL2015's concentration is low, and also about 2σ below the theoretical predictions of Dolag et al. (2004), a value still in the range of values that we expect to see in samples.

3.4. What causes the low X-ray luminosity of CL2015?

We now show that, when compared to clusters of the same mass at the overdensity $\Delta = 2500$, CL2015 is a normal object. Furthermore, we show that the low X-ray luminosity of CL2015 is due to the low total mass in the inner part of the cluster compared to other clusters of the same mass at $\Delta = 500$ and to the different dependence of mass and luminosity with radius (most of the mass within r_{500} is close to r_{500} while most of the X-ray photons come from $r \ll r_{500}$).

To show this, we compare CL2015 to the 43 groups and clusters in Sun et al. (2009). Sun et al. (2009) estimate masses assuming hydrostatic equilibrium, which limits them to consider only morphologically relaxed clusters. Figure 12 shows the distribution of entropy, temperature, and enclosed gas fraction for the cluster sample in Sun et al. (2009) as a function of $M_{2500,HE}$.
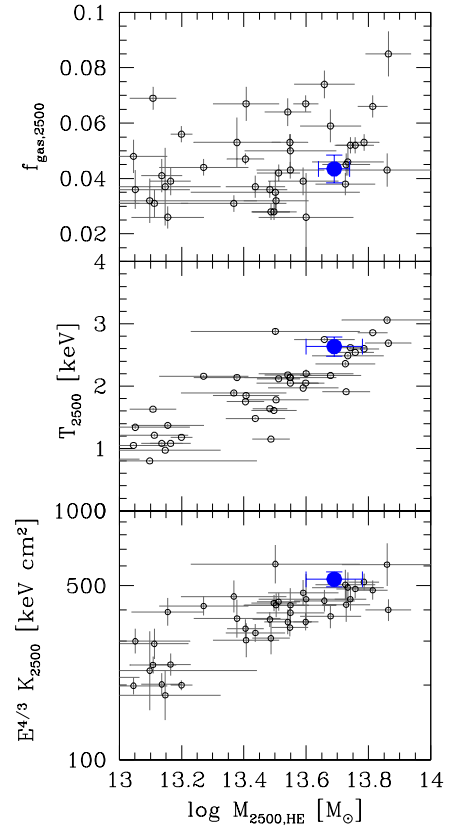

Fig. 12. Enclosed gas fraction (*top panel*), temperature (*middle panel*), and entropy (*bottom panel*) at $r_{2500,HE}$ of CL2015 (solid blue point) and of relaxed groups and clusters in Sun et al. (2009, open points).

The position of CL2015 in these plots is entirely consistent with the other clusters. In other words, CL2015 is not gas poor, or an outlier, relative to other clusters of similar mass at overdensity $\Delta = 2500$.

CL2015 becomes an outlier when its different concentration plays a role. This is because other clusters with the same mass at $\Delta = 500$ have a much larger M_{2500}. For a normal gas fraction, the lower M_{2500} results in a low gas mass and a low X-ray luminosity. With all other properties fixed, a deficit of $\sim 5.5 (= (4.7/2)^2)$ in L_X is expected, which is comparable to what is observed (Fig. 1). A better estimate of this deficit would require taking into account the concentration at all radii, rather than at r_{2500} only.

We conclude that CL2015 stands out in the $L_{X,500,ce}$ vs. M_{500} relation because although these quantities are integrated on the same radial range, this does not suffice to remove the difference dependency with radius of luminosity and mass: most of the X-ray photons are emitted from regions at small radii, while most of the mass is at larger radii. Integrating within the same radial range, $0.15 < r/r_{500} < 1$, does not completely remove these dependencies. Once concentration is factored out by considering clusters of the same mass at the radius r_{2500} at which differential quantities are measured, CL2015 falls within the distribution in temperature and entropy occupied by the Sun et al. (2009) clusters (Fig. 12). This also holds true for enclosed gas density because most of the gas mass is close to the outer integration radius.

3.5. Independent proof: The SZ view

We can test whether our explanation of the outlier position of CL2015 is valid by looking at scaling relations of the X-ray luminosity with another quantity that has a different dependence
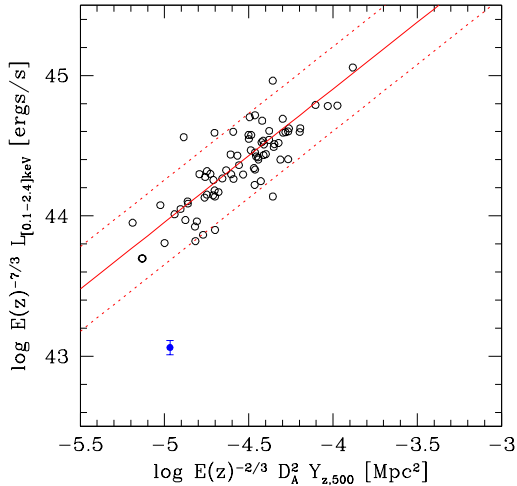
Fig. 13. X-ray luminosity vs. integrated pressure parameter. The blue point is CL2015, open points are $z < 0.2$ clusters in both the REFLEX and Planck Collaboration XXIX (2014) catalogs. The dashed corridor indicates $\pm$ a factor of two.

with radius, such as the integrated Compton parameter, that is, integrated pressure. Since pressure is proportional to n_e, while $L_X \propto n_e^2$, the integrated pressure depends on the integrated gas mass, which is a steeply growing function almost unaffected by a deficit of mass at the center, which instead strongly affects L_X, suggesting that CL2015 could be an outlier also in the $L_X - Y_{SZ}$ plane.

Figure 13 shows the L_X vs. $Y_{z,500}$ for REFLEX clusters with $z < 0.2$ (Böhringer et al. 2004) in the Planck Collaboration XXIX (2014) catalog (open points). The red solid line is the relation expected for REXCESS clusters, as calculated in Planck Collaboration IX (2011). CL2015 is detected by *Planck* (Planck Collaboration XXIX 2014) and is also plotted in the figure (blue solid point) with the X-ray luminosity converted from the [0.5–2] keV *Swift* value. CL2015 is an obvious outlier in the $L_X - Y_{500}$ plane. This was also noted in Planck Collaboration XXVII (2016), where it was considered "X-ray underluminous" for its SZ strength based on an X-ray luminosity (presumably un upper-limit, not listed) from Rosat All Sky Survey data.

To summarize, CL2015 is an obvious outlier compared to easy-to-detect (REXCESS, REFLEX, *Planck*) clusters in scaling relations involving X-ray luminosity (measured by three different teams from three different X-ray telescopes) vs. dynamical mass (measured by two teams in three different ways) or integrated pressure (measured by two teams). This reassures us that the outlier status of CL2015 is not a telescope temporary failure or a momentary lapse of reason on the part of the author. The low concentration is the ultimate reason for CL2015's outlier status in quantities that weight cluster-centric radii in different ways (namely $L_{X,500,ce} - M_{500}$ and $L_X - Y_{z,500}$) and also its normal behaviour for differential measurements performed at the same radius (namely, $T_{2500} - M_{2500}$, $K_{2500} - M_{2500}$) or close radii ($f_{gas,2500} - M_{2500}$).

We emphasize once more that CL2015, at $\sim -1.5\sigma$ from the relation in an X-ray unbiased sample, is not an outlier in that distribution. The rarity of outliers in $L_X - Y_{SZ}$ or $L_X - M_{500}$ when easy-to-detect cluster samples are considered is related to the difficulty of having such type of objects in samples because of their low X-ray luminosity for their M_{500} and also their low SZ signal. CL2015 is at the very boundary of the *Planck* detection limit: it is detected at the threshold of one of the detection codes

($S/N = 4.57$, MMF1, Planck Collaboration XXVII 2016) and below the threshold of a different implementation of the matched multifilter code (MMF3). No other XUCS clusters of low X-ray luminosity for their mass or with $\log M_{gas,500}/M_\odot < 13.1$ are detected by *Planck*. Therefore, even *Planck* is missing clusters with $\log M_{500}/M_\odot \approx 14.3$ unless they have a gas fraction larger than CL2015.

3.6. One more test: Stellar content

An alternative test to support our suggestion of a shallower mass distribution in CL2015 relative to other clusters can be done by checking that it is not an outlier in diagrams based on quantities with similar dependence with radius. Since both galaxies and dark matter are collisionless, stellar mass is expected to be distributed as dark matter, as generally found in weak-lensing analyses of clusters at intermediate redshift (e.g., Hoekstra et al. 1998; Kneib et al. 2003) and tested in detail for a few clusters (Andreon 2015). Therefore, most of the stellar mass is at large cluster-centric radii, like the total mass. We expect therefore a normal stellar fraction for CL2015.

Stellar masses have been derived from r band luminosity of red-sequence galaxies within $r_{500,cau}$, as done for the clusters to which we compare CL2015 (Andreon 2010, 2012, to which we defer for details). In short, we used $r < 19$ mag photometry from the 14th Sloan Digital Sky Survey (SDSS) data release (Abolfathi et al. 2018), we selected galaxies within 0.1 mag redward and 0.2 mag blueward of the $g-r$ color–magnitude relation, and we fit, without binning, the luminosity function accounting for background, estimated in adjacent lines of sight outside the cluster turnaround radius, assuming uniform priors for the parameters, a Schechter (1976) function for cluster galaxies, a power law for background galaxies, and the likelihood expression in Andreon et al. (2005). Since BCGs might not be drawn from the Schechter function because of their possibly different formation history, we removed the BCG from the fitted sample and we added back its flux to the integral of the luminosity function (as in Andreon 2010). Figure 14 shows the counts in the cluster and control field directions (top panel); the cluster contribution is given by the difference of these two, shown in the middle panel. The BCG (leftmost point), IC 1602, is about 2 mag brighter than other galaxies, which is the minimum difference needed to call the system a "fossil" cluster (Jones et al. 2003). In this respect, CL2015 is not unusual: among the 42 X-ray selected clusters studied in Andreon (2010), six (about 15%) have a similar magnitude difference with the other cluster galaxies. In the much larger sample of Lauer et al. (2014), IC 1602 is 1σ brighter than the average BCG and its central velocity dispersion is in line with its central luminosity (i.e., it obeys the Faber & Jackson (1976) relation when applied to central quantities).

The bottom panel of Fig. 14 shows the contribution of each luminosity bin to the total flux, showing that faint bins contribute little to the total flux, meaning that the data used are adequate for our purposes. The total flux (the integral of L times the luminosity function) is then corrected by 15% for missing light, converted to stellar mass assuming the M/L derived by Cappellari et al. (2006), and deprojected assuming a Navarro et al. (1997) profile with a light concentration of three, as for the clusters to which we are comparing. We found a stellar mass of $\log M_{500,*} = 12.50 \pm 0.08\,M_\odot$.

Figure 15 compares CL2015 to other clusters: X-ray relaxed clusters (from Andreon 2012) and a random sampling of a X-ray flux-limited sample (from Andreon 2010), the latter binned to emphasize the trend by reducing the scatter around the

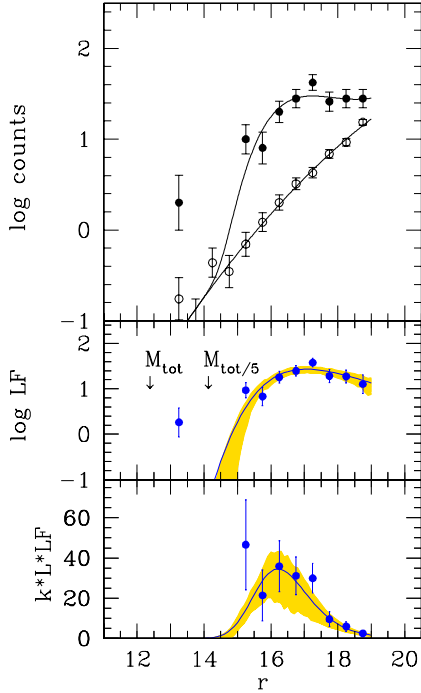**Fig. 14.** Luminosity Function determination. *Upper panel*: galaxy log counts in the CL2015 direction (solid dots), in an adjacent line of sight for background estimation (open dots). The cluster contribution is given by the difference of the two counts, shown in the *middle panel*, which also reports the integral of the luminosity function ($M_{\rm tot}$) and 1/5th of it ($M_{\rm tot/5}$). The *bottom panel* gives the luminosity contribution of each magnitude bin (in arbitrary units). Curves mark the fitted model to un-binned data, after removal of the brightest cluster galaxy. Approximated point errors (computed with the usual sum in quadrature) are marked with bars; precisely computed 68% errors on the model are shaded.
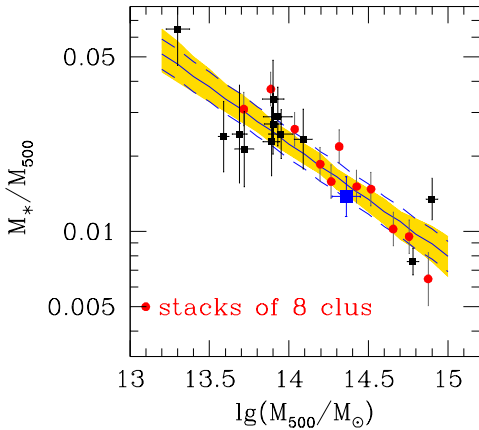

Fig. 15. Stellar fraction of CL2015 (solid blue square) compared to other clusters: (a) X-ray relaxed clusters (black points) from Andreon (2012), with stellar mass of Abell 2029 updated in Renzini & Andreon (2014). The solid line is the mean model, while the shading indicates the 68% uncertainty (highest posterior density interval). The dashed corridor is the mean model ± the intrinsic scatter. (b) X-ray selected clusters (red points), after averaging in bins of eight clusters each to emphasize the mean trend while reducing the scatter around the mean relation.

mean relation. The fit to X-ray relaxed clusters (solid line) uses the same fitting code used in Andreon (2012). The stellar fraction of CL2015 within $\Delta = 500$ (blue square) is consistent with that of the other clusters. This indicates that in spite its low concentration, CL2015 has a normal stellar fraction. The normal stellar
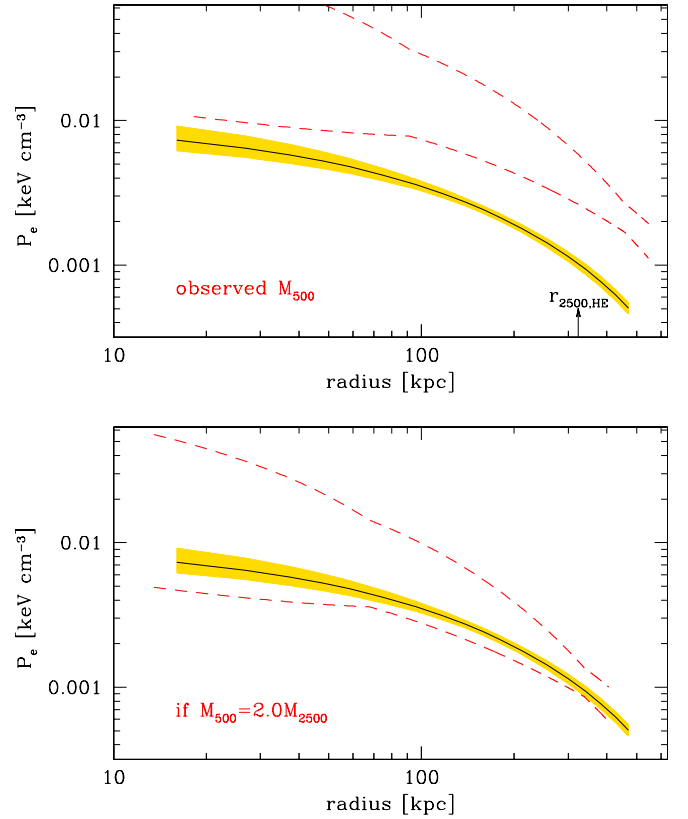

Fig. 16. Pressure profile of CL2015 (line, the shading marks the 68% uncertainty) vs. the $\pm2\sigma$ range of REXCESS clusters scaled at the CL2015 mass (*top panel*) and at the mass $M_{500} = 2.0\,M_{2500}$ (*bottom panel*) typical of clusters of normal concentration.

fraction is what we expected for a cluster with any concentration because concentration is irrelevant for a comparison among quantities distributed as mass. The normal stellar fraction provides an independent test of our conclusion that concentration is driving the different shining of CL2015.

3.7. Pressure and density profile comparisons before and after factoring out the unusual concentration

In this section we want to show that, once differences in concentration are taken into account, CL2015 displays the same pressure profile as other clusters. Figure 16 compares the pressure profile of CL2015 (solid line with shading marking the 68% uncertainty) with the universal pressure profile and its $\pm2\sigma$ range derived from REXCESS clusters (Arnaud et al. 2010). In the top panel, we scaled the universal profile to the mass of CL2015 at overdensity $\Delta = 500$. CL2015's profile is systematically below the -2σ range, meaning it has a pressure systematically and significantly lower than any of the REXCESS clusters, hence breaking the universality of the pressure profile. However, the mass inside the radial range in which pressure is measured is different for CL2015 and REXCESS clusters because $M_{500} = 4.7\,M_{2500}$ for CL2015 and $M_{500} = 2.0\,M_{2500}$ for the others. To (approximatively) factor out the effect of concentration we therefore use $M_{500} = 2.0\,M_{2500}$ also for CL2015 (i.e., we effectively use M_{2500} to rescale all clusters). The bottom panel shows that CL2015's pressure profile is enclosed in the $\pm2\sigma$ range of REXCESS clusters. The unusual pressure profile is largely driven by the unusual concentration.
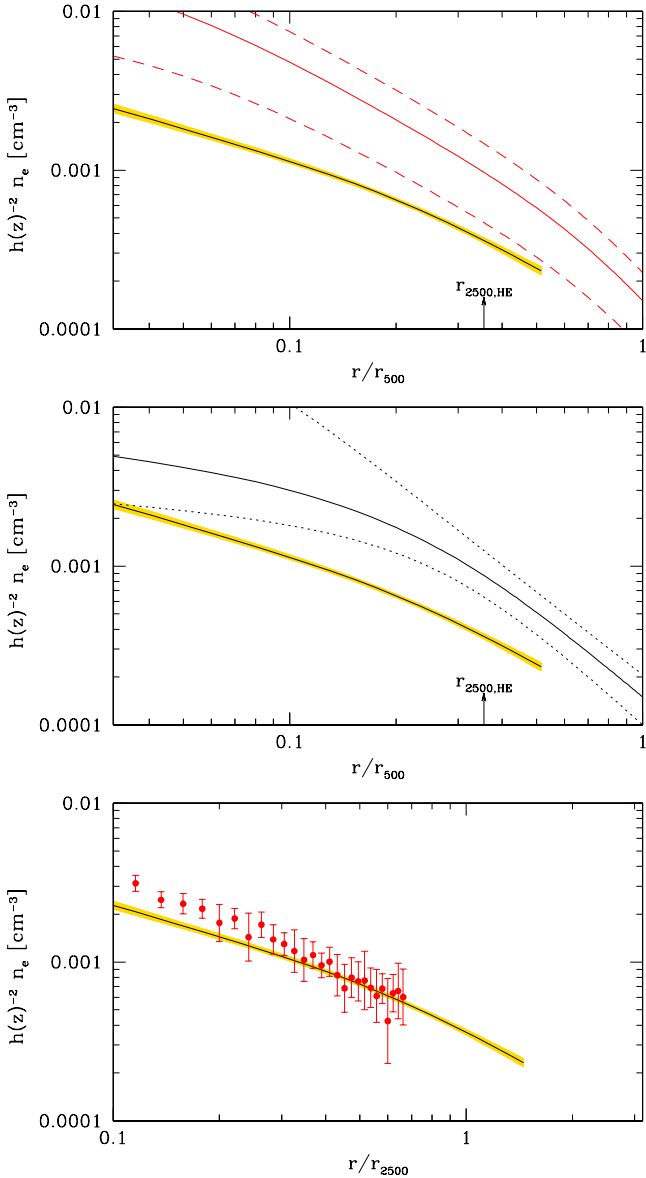
Fig. 18. Giant Metrewave Radio Telescope 400 MHz image of the central part (about 0.1% of the imaged area) of CL2015. The rms near the source is $\sim100\,\mu$Jy beam^{-1} and the resolution of the image is 8.3×5.0 arcsec at 50 deg position angle. The (optical) BCG position is coincident with the brightest radio spot, at (RA,Dec) = (0:55:51.9,$-$9:59:08). The color scale has Jy beam^{-1} units.

Fig. 17. Electron pressure profile of CL2015 (line, the shading marks the 68% uncertainty) vs. the $\pm2\sigma$ range of XCOP clusters (*top panel*), *Planck*-selected clusters (*middle panel*), and of Abell 744, a cluster with the same M_{2500} (*bottom panel*).

(points from Cavagnolo et al. 2009; r_{2500} from Sun et al. 2009). This object has been selected as the object closest to CL2015 in entropy, temperature, and gas fraction among those in Fig. 12. However, this cluster lacks r_{500} estimates and therefore we ignore if it is another cluster of low concentration, or a cluster of low M_{500} mass.

3.8. Radio

We observed CL2015 with the upgraded Giant Metrewave Radio Telescope (uGMRT, Gupta et al. 2017) in band-3 (250–500 MHz) for approximately three net hours of integration. The data were recorded with 200 MHz bandwidth (300−500 MHz) and 4096 channels. The data were analyzed in a fully automated Common Astronomy Software Application-based pipeline (Ishwara-Chandra et al., in prep.[1]) using standard wideband analysis procedures, which include setting flux scale using the primary calibrator 3C48, bandpass, and gain calibration and transferring the flux scale to the science target via the phase calibrator. After the gain calibration, the data were averaged with the post-averaged channel width of $\sim$0.5 MHz before split, to keep the bandwidth smearing negligible. The science target was imaged using the CASA task `tclean` following wideband multi-frequency synthesis procedures. Four iterations of phase-only self-calibration were performed, followed by four iterations of amplitude and phase self-calibration. During self-calibration, flagging was performed on the residuals for a better result. The resolution and rms of the image are 8.3×5.0 arcsec at 50 deg position angle and $\sim$100 μJy beam^{-1} near the central source.

The central radio source (Fig. 18), spatially coincident with the BCG of CL2015, IC 1602, is a double-lobed source with complex morphology. The radio jets show several knots and twists, which could be due to an inhomogenous medium.

Figure 17 repeats much of the same exercise, but for the electron density profile: the top panel compares the electron density profile of CL2015 to the universal density profile and its $\pm2\sigma$ range derived from X-COP clusters (Ghirardini et al. 2019). CL2015's profile is systematically below the -2σ range, that is, it is systematically and significantly lower than any of the X-COP clusters. We verified that the same holds true using a mass-matched sample of 19 clusters in REXCESS using electron density profiles in Croston et al. (2009). The middle panel shows that CL2015's electron density profile is even lower than *Planck*-selected clusters (from Planck Collaboration IX 2011).

However, electron density is low because the compared clusters have a normal concentration while CL2015 has a low concentration. CL2015's electron density profile matches other cluster profiles within r_{2500} if one chooses a comparison cluster with the same mass within this overdensity, as illustrated by the bottom panel where we compare CL2015 to Abell 744
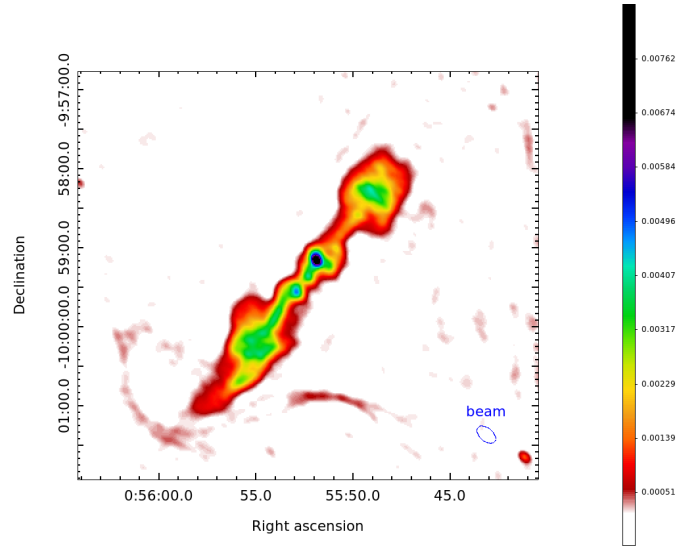
---

[1] See also http://www.ncra.tifr.res.in/~ishwar/pipeline.html
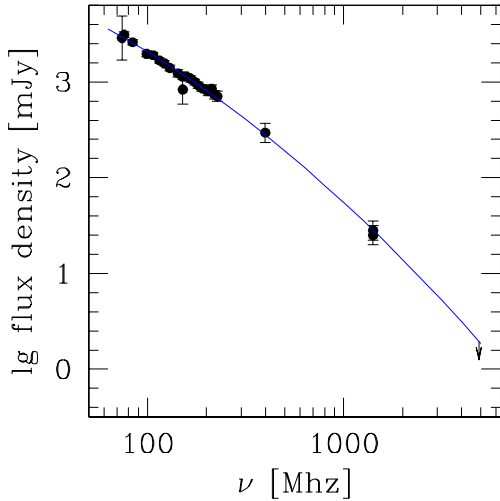
Fig. 19. Radio spectrum of the BCG of CL2015, IC 1602. The curve has the equation: $\log f = -0.315934 \log^2 \nu + 0.00838119 \log \nu + 4.56086$.

The linear extent of the source is about 120 kpc radius (about $r_{2500}/3$), the radio luminosity at 400 MHz is 2×10^{24} WHz^{-1}, and the radio flux is ~295 mJy. At 1.4 GHz IC 1602 is faint, but still in the range of other cluster radio sources, for example, those in Owen & Ledlow (1997).

When combined with GMRT observations at 153 MHz (Intema et al. 2017), Very Large Array Low-Frequency Survey at 74 MHz (Cohen et al. 2007), Very Large Array at 1.4 GHz (Owen & Ledlow 1997), Murchison Widefield Array (MWA) at several bands from 76 to 227 MHz Hurley-Walker et al. (2017), NRAO VLA Sky Survey at 1.4 GHz (Condon et al. 1998), and the upper limit at 4.8 GHz Lin et al. (2009), the spectrum of the whole source shows a curvature with a clear steepening towards high frequencies (Fig. 19). The spectral index at the low frequency part (74 MHz till 400 MHz) is ~1.3, whereas it is ~2 in the frequency range 400 MHz−4.86 GHz. Such a curved spectrum with steep spectral index is typical of source relics (e.g., Brienza et al. 2016). We suspect the radio source has undergone episodic jet activity and the relic plasma from the previous jet activity is primarily radiating at low radio frequencies causing the excess flux. The presence of diffuse emission beyond the "hotspots" on either side could be the relic emission from the active galactic nucleus which is responsible for steep spectra.

Although an AGN is present at the cluster center and we see radio lobes, its effect on the X-ray gas is not discernable in our X-ray data: we see no cavities, no rims surrounding them, no sharp break in the surface brightness profile, no azimuthal asymmetry, all of which are seen, for example, in Abell 2390 (Vikhlinin et al. 2006), however using higher resolution *Chandra* data. The presence of an AGN at the center of the cluster might lower the gas fraction in the cluster center by displacing the gas at larger radii (but it should produce X-ray cavities that we do not see). It might also bias our estimate of the gas fraction to the high end if it provides non-thermal pressure support to the gas (not accounted for in our hydrostatic analysis). Given that gas fraction is normal at $\Delta = 2500$ (Sect. 3.5), and also consistent with Vikhlinin et al. (2006) clusters of the same temperature, deviations from hydrostatic equilibrium should be small unless there is fine tuning between the amount of gas displaced and the mass overestimate.

An interesting feature is the "S"-shaped narrow but long shock-like feature at the end of southeastern lobe (see Fig. 18). This is clearly disconnected from the rest of the radio source.
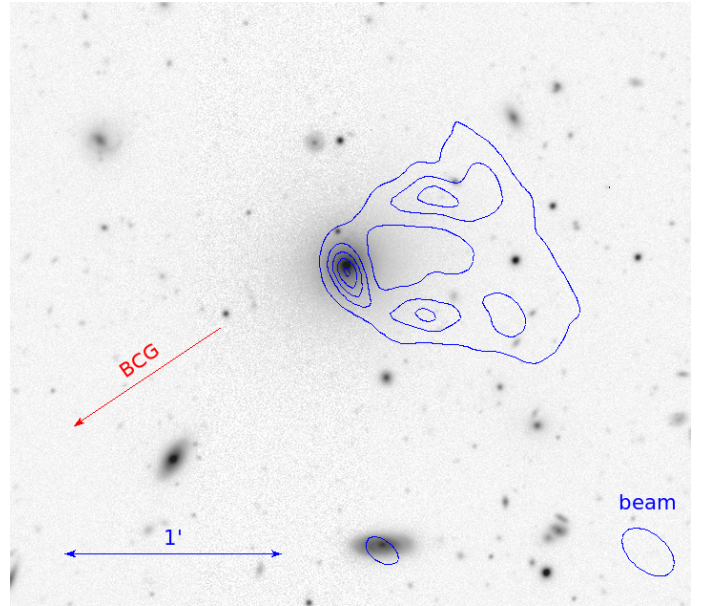

Fig. 20. DECam Legacy survey (Dey et al. 2019) r-band image with GMRT 400 MHz contours of the head tail source. The galaxy has J2000 coordinates (RA,Dec) = (0:55:32.5,−9:56:27). North is up and east is to the left. Contours are in steps of 1 mJy beam^{-1} starting from 0.3 mJy beam^{-1}.

The detailed investigation of this arc requires much deeper multiwavelength observations and is beyond the scope of this paper.

Figure 20 shows a low luminosity head tail source 5.5′ northwest of the cluster center, centered on a spectroscopically confirmed cluster member (at 0:55:32.5,−9:56:27). The flux density of the source at 400 MHz is 53 mJy. The source is also detected in NVSS (Condon et al. 1998) with a flux density of 23.9 mJy. The source is barely detected in MWA (Hurley-Walker et al. 2017) and not detected in GMRT Sky Survey (Intema et al. 2017) and this gives the spectral index of ~0.7. The large field of view of the GMRT image allows us to easily spot at least five more clusters in the field of view of ~2 deg^2 centered on CL2015, which will be reported elsewhere.

4. Discussion

Cluster mass can be estimated in several ways, for example, from the escape velocity, which does not make assumptions on cluster status (caustics, Diaferio 1999; Serra et al. 2011), from velocity dispersions assuming dynamical equilibrium, or from X-ray data assuming hydrostatic equilibrium. If the cluster is out of equilibrium, these estimates tend to disagree with each other. In particular, in a system that has experienced a recent merger, mass estimates from velocity dispersion and caustic should differ each other, except if the merger occurs close to the plane of the sky. Mergers close to the plane of the sky are those easier to recognize from the unrelaxed X-ray cluster morphology (e.g., Takizawa et al. 2010) and from the positional offset between the (collisional) gas and the (collisionless) galaxies. Independently from the merger direction, in out-of-equilibrium clusters the X-ray mass based on hydrostatic equilibrium tends to underestimate the true mass because of the neglected pressure support (e.g., Rasia et al. 2004; Takizawa et al. 2010). Therefore, X-ray morphology and different estimates of mass allow us to recognize the presence of a recent merger. Both the regular X-ray morphology of CL2015 and the coincidence of the X-ray

center with the BCG location exclude a merger close to the plane of the sky. The agreement between masses derived from caustic and velocity dispersion (most sensitive to a merger along the line of sight) excludes a merger with a component along the line of sight. Finally, the agreement between hydrostatic and dynamical masses excludes a strong non-thermal support, including a merger. A merger along the line of sight is also the easiest to recognize in redshift-space diagrams and none is seen (also shown in Fig. 9 of Abdullah et al. 2018). Therefore, a recent merger can be excluded, and cannot be invoked to explain the low X-ray emission and low concentration of CL2015. While not viable for CL2015, mergers could provide an explanation for other XUCS clusters with low X-ray emission, for example for CL3000, which shows an offset between the gas and the galaxies, a bit like the Bullet cluster (Andreon et al. 2016).

Neither the presence of a bright BCG, nor the cluster being classified as fossil, explain the low X-ray emission and low concentration of CL2015, because other clusters in XUCS are X-ray faint for their mass but do not have a similar luminosity difference between the first and second members, and because the BCG has a luminosity typical of other BCGs.

CL2015 is perhaps the first known cluster with a mass concentration as low as $c_{500} = 1.5$. It should not be seen, however, as an anomaly: the rarity of such objects in X-ray selected observational samples is not an indication of their rarity in the real Universe because their low central mass induces a very low X-ray luminosity that makes them hard to include in observational X-ray selected samples. On the other hand, CL2015 is just 1.5σ away from the mean luminosity for its mass in an X-ray unbiased sample, meaning it is not unusual at all. It is interesting to note that the shear-selected sample of Miyazaki et al. (2018) has an average concentration of $c_{500} = 2.4 \pm 0.5$, lower than the common $c_{500} = 4.2$ value obtained for X-ray selected clusters, hence supporting the idea that low concentration clusters are more common in samples not affected by the X-ray bias. One might be tempted to define CL2015 as "underluminous" when compared to X-ray clusters. However, this label assumes that clusters such as CL2015 are the exception in the Universe, while X-ray selected clusters represent the norm. When compared to an X-ray unbiased sample, CL2015 is just 1.5σ away from the mean luminosity for its mass, therefore cannot be labeled "underluminous". Recent works (see Introduction) now agree that clusters that enter more easily in X-ray-selected samples are "too bright" (e.g., virtually all clusters in the complete, X-ray selected sample of Giles et al. 2017 are brighter than the average for their mass).

Among the new cluster population that has been discovered in recent years, CL2015 has a unique dataset. Pearson et al. (2017) presents several optically-selected groups that are X-ray faint for their mass, where however these mass estimates comes from galaxy counts (similar to Andreon & Moretti 2011). Better estimates of mass are required to confirm these clusters as truly faint for their mass. Similarly, Planck Collaboration XXVII (2016) and Rossetti et al. (2017) found clusters possibly underluminous for their integrated pressure parameter, but they need masses (and also deeper X-ray data in the case of Planck Collaboration XXVII 2016) to confirm them as faint for their mass, or as having a low mass concentration. Xu et al. (2018) discovered groups with a low surface brightness X-ray emission (more precisely, more extended than a cluster model scaled down to have the observed group luminosity). However, lacking precise mass estimates they cannot investigate the reason for the low surface brightness, whether this is due to a low total mass concentration or to a reduced gas fraction in the center. Furthermore, because of the shallowness of the X-ray data, the detection

of clusters of low surface brightness like CL2015 is precluded to them, and indeed CL2015 is not in their sample. As a consequence, their detected objects are expected to sample a narrower range in surface brightness than the XUCS sample.

5. Conclusions

In recent years, the known variety of galaxy clusters has been constantly increasing, as testified by the increasing scatter displayed by the scaling relations, by a larger spread in gas fraction, and by the discovery of clusters with low electron density profiles. In this context, we obtained a 58 ks *Swift* XRT observation, a GMRT band-3 10.8 ks exposure, and we collected archival data from *Einstein*, *Planck*, and SDSS on CL2015, an intermediate mass cluster ($\log M_{500}/M_\odot = 14.39 \pm 0.09$) in the nearby Universe. The cluster was selected because it has a low X-ray luminosity ($L_{X,500,ce} = 42.79 \pm 0.06$ in the [0.5,2] keV band) for its mass M_{500}, about $\sim 12\sigma$ below the mean relation for an X-ray selected sample, yet only $\sim 1.5\sigma$ below the mean of an X-ray unbiased sample.

CL2015 is not an outlier because of faulty X-ray luminosities, because values derived by different X-ray telescopes and teams agree with each other. Faulty masses are also not the cause, because the hydrostatic mass we derive from XRT agrees with three dynamical estimates derived by two independent teams, and because CL2015 is also an outlier in a scaling that replaces mass with an integrated pressure parameter. A recent merger is not the cause, because such an event is ruled out by X-ray and dynamical data.

Universal profiles are deeply rooted in our understanding of clusters. For example, the *Planck* cluster detection algorithm assumes a universal pressure profile for all clusters, and pressure (the integral of the pressure profile) is perhaps the current most appealing mass proxy. The pressure and the electron density profiles of CL2015 are systematically outside the $\pm 2\sigma$ range of the universal profiles, with the electron density profile being even lower than that of *Planck*-selected clusters. CL2015 turns out also to be an outlier in the X-ray luminosity vs. SZ strength, but a normal object in terms of stellar mass fraction.

CL2015's hydrostatic mass profile, by itself or when it is considered together with dynamical masses, shows that the cluster has a remarkably low concentration and different sparsity compared to clusters in X-ray selected samples. CL2015 has a $c_{500} = 1.5 \pm 0.4$ vs. a typical $c_{500} = 4.2$, and $M_{500}/M_{2500} = 4.7$ vs. a typical value of 2.0. The unusual concentration and (inverse) sparsity makes CL2015 an outlier in scaling relations involving integrated quantities with different radial dependencies, such as $L_{X,500,ce} - M_{500}$ and $L_X - Y_{SZ}$, even when they are measured inside the same radial range. This is confirmed by the evidence that CL2015 is not an outlier in relations involving quantities with similar dependencies with radius, like stellar mass vs. total mass. Furthermore, when concentration differences are accounted for, the properties of CL2015 become consistent with comparison samples, for example, enclosed gas fraction, X-ray temperature, and entropy at R_{2500}, and the pressure profile falls in the range of the "universal" profile derived for X-ray selected clusters.

The different sensitivity of various observables to radius is promising for the collection of larger samples of low concentration clusters, for example looking for outliers combining quantities mostly sensitive to small radii, such as L_X, to quantities which instead continue to grow with increasing radius (or decreasing Δ), such as total mass, SZ strength, or stellar mass.

CL2015 is perhaps the first known cluster with such a low concentration and high quality data. It should not be seen,

however, as an anomaly: the rarity of such objects in observational samples is not an indication of their infrequency in the real Universe because their low X-ray luminosity makes it difficult for them to be included in observational samples. As we discuss, while CL2015 is an outlier relative to X-ray selected samples, its low luminosity is shared by other clusters of similar mass in the X-ray unbiased sample of Andreon et al. (2016), and a few other X-ray faint clusters relative to their SZ strength in Planck Collaboration XXVII (2016: one such cluster is indeed CL2015).

References

Abdullah, M. H., Wilson, G., & Klypin, A. 2018, ApJ, 861, 22
Abell, G. O. 1958, ApJS, 3, 211
Abolfathi, B., Aguado, D. S., Aguilar, G., et al. 2018, ApJS, 235, 42
Anders, E., & Grevesse, N. 1989, Geochim. Cosmochim. Acta, 53, 197
Andreon, S. 2010, MNRAS, 407, 263
Andreon, S. 2012, A&A, 548, A83
Andreon, S. 2015, A&A, 575, A108
Andreon, S., & Hurn, M. 2013, Stat. Analys. Data Min., 9, 15
Andreon, S., & Moretti, A. 2011, A&A, 536, A37
Andreon, S., Punzi, G., & Grado, A. 2005, MNRAS, 360, 727
Andreon, S., Maughan, B., Trinchieri, G., & Kurk, J. 2009, A&A, 507, 147
Andreon, S., Trinchieri, G., & Pizzolato, F. 2011, MNRAS, 412, 2391
Andreon, S., Serra, A. L., Moretti, A., & Trinchieri, G. 2016, A&A, 585, A147
Andreon, S., Wang, J., Trinchieri, G., Moretti, A., & Serra, A. L. 2017, A&A, 606, A24
Arnaud, M., Pointecouteau, E., & Pratt, G. W. 2005, A&A, 441, 893
Arnaud, M., Pratt, G. W., Piffaretti, R., et al. 2010, A&A, 517, A92
Böhringer, H., Schuecker, P., Guzzo, L., et al. 2004, A&A, 425, 367
Brienza, M., Godfrey, L., Morganti, R., et al. 2016, A&A, 585, A29
Cappellari, M., Bacon, R., Bureau, M., et al. 2006, MNRAS, 366, 1126
Cavagnolo, K. W., Donahue, M., Voit, G. M., & Sun, M. 2009, ApJS, 182, 12
Cohen, A. S., Lane, W. M., Cotton, W. D., et al. 2007, AJ, 134, 1245
Condon, J. J., Cotton, W. D., Greisen, E. W., et al. 1998, AJ, 115, 1693
Corasaniti, P. S., Ettori, S., Rasera, Y., et al. 2018, ApJ, 862, 40
Croston, J. H., Kraft, R. P., Hardcastle, M. J., et al. 2009, MNRAS, 395, 1999
Dey, A., Schlegel, D. J., Lang, D., et al. 2019, AJ, 157, 168
Diaferio, A. 1999, MNRAS, 309, 610
Diaferio, A., & Geller, M. J. 1997, ApJ, 481, 633
Dolag, K., Bartelmann, M., Perrotta, F., et al. 2004, A&A, 416, 853
Ettori, S., Ghirardini, V., Eckert, D., et al. 2019, A&A, 621, A39
Evrard, A. E., Bialek, J., Busha, M., et al. 2008, ApJ, 672, 122
Faber, S. M., & Jackson, R. E. 1976, ApJ, 204, 668

Ge, C., Sun, M., Rozo, E., et al. 2019, MNRAS, 484, 1946
Ghirardini, V., Eckert, D., Ettori, S., et al. 2019, A&A, 621, A41
Giles, P. A., Maughan, B. J., Hamana, T., et al. 2015, MNRAS, 447, 3044
Giles, P. A., Maughan, B. J., Pacaud, F., et al. 2016, A&A, 592, A3
Giles, P. A., Maughan, B. J., Dahle, H., et al. 2017, MNRAS, 465, 858
Hoekstra, H., Franx, M., Kuijken, K., & Squires, G. 1998, ApJ, 504, 636
Hurley-Walker, N., Callingham, J. R., Hancock, P. J., et al. 2017, MNRAS, 464, 1146
Intema, H. T., Jagannathan, P., Mooley, K. P., & Frail, D. A. 2017, A&A, 598, A78
Jones, C., & Forman, W. 1999, ApJ, 511, 65
Jones, L. R., Ponman, T. J., Horton, A., et al. 2003, MNRAS, 343, 627
Kalberla, P. M. W., Burton, W. B., Hartmann, D., et al. 2005, A&A, 440, 775
Kneib, J.-P., Hudelot, P., Ellis, R. S., et al. 2003, ApJ, 598, 804
Lauer, T. R., Postman, M., Strauss, M. A., Graves, G. J., & Chisari, N. E. 2014, ApJ, 797, 82
Lin, Y.-T., Partridge, B., Pober, J. C., et al. 2009, ApJ, 694, 992
Mantz, A. B., Allen, S. W., Morris, R. G., et al. 2016, MNRAS, 463, 3582
Maughan, B.J., Giles, P. A., Randall, S. W., et al. 2012, MNRAS, 421, 1583
McDonald, M., Benson, B. A., Vikhlinin, A., et al. 2014, ApJ, 794, 67
Miyazaki, S., Oguri, M., Hamana, T., et al. 2018, PASJ, 70, S27
Moretti, A., Pagani, C., Cusumano, G., et al. 2009, A&A, 493, 501
Mushotzky, R. F., Aird, J., & Barger, A. J. 2019, Astro2020 Decadal Survey [arXiv:1903.04083]
Navarro, J. F., Frenk, C. S., & White, S. D. M. 1997, ApJ, 490, 493
Owen, F. N., & Ledlow, M. J. 1997, ApJS, 108, 41
Pacaud, F., Pierre, M., Adami, C., et al. 2007, MNRAS, 382, 1289
Pearson, R. J., Ponman, T. J., Norberg, P., et al. 2017, MNRAS, 469, 3489
Pointecouteau, E., Arnaud, M., & Pratt, G. W. 2005, A&A, 435, 1
Planck Collaboration IX. 2011, A&A, 536, A9
Planck Collaboration IX. 2012, A&A, 543, A102
Planck Collaboration III. 2013, A&A, 550, A129
Planck Collaboration XXIX. 2014, A&A, 571, A29
Planck Collaboration XXVII. 2016, A&A, 594, A27
Pratt, G. W., & Arnaud, M. 2005, A&A, 429, 791
Pratt, G. W., Croston, J. H., Arnaud, M., & Böhringer, H. 2009, A&A, 498, 361
Pratt, G. W., Arnaud, M., Piffaretti, R., et al. 2010, A&A, 511, A85
Rasia, E., Tormen, G., & Moscardini, L. 2004, MNRAS, 351, 237
Renzini, A., & Andreon, S. 2014, MNRAS, 444, 3581
Rossetti, M., Gastaldello, F., Eckert, D., et al. 2017, MNRAS, 468, 1917
Sanders, J. S., Fabian, A. C., Russell, H. R., & Walker, S. A. 2018, MNRAS, 474, 1065
Schechter, P. 1976, ApJ, 203, 297
Serra, A. L., Diaferio, A., Murante, G., & Borgani, S. 2011, MNRAS, 412, 800
Smith, R. K., Brickhouse, N. S., Liedahl, D. A., & Raymond, J. C. 2001, ApJ, 556, L91
Stanek, R., Evrard, A. E., Böhringer, H., et al. 2006, ApJ, 648, 956
Sun, M., Voit, G. M., Donahue, M., et al. 2009, ApJ, 693, 1142
Sun, M., Sehgal, N., Voit, G. M., et al. 2011, ApJ, 727, L49
Takizawa, M., Nagino, R., Matsushita, K., et al. 2010, PASJ, 62, 951
Vikhlinin, A., Markevitch, M., Murray, S. S., et al. 2005, ApJ, 628, 655
Vikhlinin, A., Kravtsov, A., Forman, W., et al. 2006, ApJ, 640, 691
Vikhlinin, A., Kravtsov, A. V., Burenin, R. A., et al. 2009, ApJ, 692, 1060
Voit, G. M., Kay, S. T., Bryan, G. L., et al. 2005, MNRAS, 364, 909
Xu, W., Ramos-Ceja, M. E., Pacaud, F., Reiprich, T. H., & Erben, T. 2018, A&A, 619, A162
Walker, S. A., Nagai, D., & Simionescu, A. 2019, Astro2020 Decadal Survey, BAAS, 51, 218
Willis, J. P., Pacaud, F., Valtchanov, I., et al. 2005, MNRAS, 363, 675
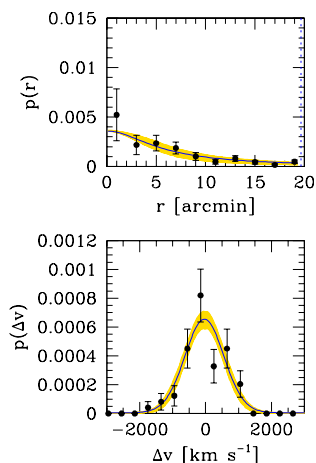
Appendix A: Mass from galaxy dynamics

Fig. A.1. Spatial and velocity distributions. *Top panel*: radial profile of the galaxies with spectroscopic redshift within $3000\,\mathrm{km\,s^{-1}}$ of CL2015's redshift. *Bottom panel*: velocity distribution of the same galaxies. In both panels, the solid line is the mean model fitted to the individual galaxy data in the r−v plane, while the shading indicates the 68% uncertainty (highest posterior density interval). Points and approximated error bars are derived by ignoring the velocity (*top panel*) or radial (*bottom panel*) information, binning galaxies in velocity bins, and adopting approximated Poisson errors, as is commonly found in the literature.

CL2015's dynamical masses have been derived in three different ways by two different teams, Abdullah et al. (2018) and Andreon et al. (2016), who, however, do not show figures for CL2015. These are shown here for completeness.

In Andreon et al. (2016) we computed the cluster velocity dispersion with a full Bayesian modeling of the data in the radius-velocity space, allowing a Gaussian velocity and a King radial profile for member galaxies and a uniform distribution in velocity and radial distance for foreground and background galaxies (see Andreon et al. 2016 for details). There are 61 spectroscopic members in CL2015. The marginal distributions are shown in Fig. A.1. The cluster members are adequately described by the model, with $\sigma_v = 595 \pm 56\,\mathrm{km\,s^{-1}}$, from which M_{200} is derived using the calibration in Evrard et al. (2008), and then M_{500} assuming a Navarro et al. (1997)'s profile with concentration 5. We found $\log M_{500,\sigma_v} = 14.27 \pm 0.12$ (Andreon et al. 2016).

Caustic masses within r_{200}, M_{200}, have been derived following Diaferio & Geller (1997), Diaferio (1999), and Serra et al. (2011), then converted into r_{500} and M_{500} assuming a Navarro et al. (1997) profile with concentration 5. We found $\log M_{500,cau} = 14.36 \pm 0.09$ (Andreon et al. 2016).

The GalWeigh technic (Abdullah et al. 2018) uses much of the same information used in the caustic mass determination (velocity and cluster-centric distance) for identifying cluster members, from which cluster masses can be derived with different sets of assumptions. Assuming a Navarro et al. (1997) profile and using spectroscopic data that overlap with those used by us, the authors found $\log M_{500,dyn} = 14.27$ (no error quoted) for CL2015. The caustic diagram of CL2015 (named A117 in their paper) is shown in their Fig. 9.

Appendix B: Test of our reduction and analysis pipeline

To test our ability to derive thermodynamic profiles vs. state-of-the-art analyses, Fig. B.1 compares the thermodynamic profiles
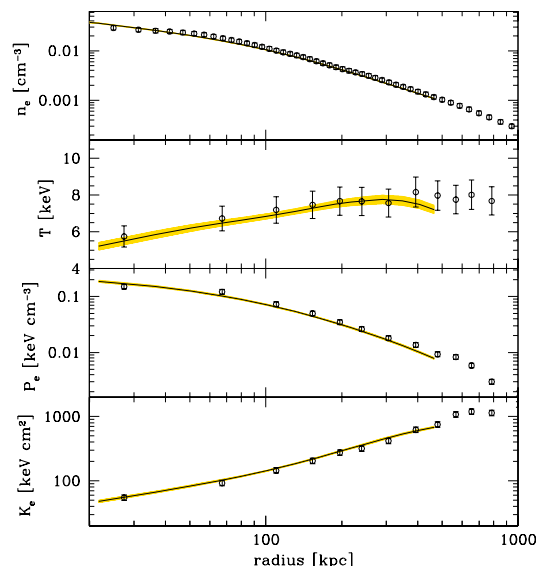

Fig. B.1. Comparison of XMM and XRT Abell 2029 thermodynamic profiles. Points indicate values derived from XMM (Ghirardini et al. 2019) while error bars indicate ±10% (statistical errors are negligible), whereas our XRT mean model is indicated with a solid line and shading (marking 68% intervals).

of Abell 2029 derived by us using 58 ks of *Swift* data with those derived using ~170 ks of *XMM-Newton* data by Ghirardini et al. (2019). The angular size of Abell 2029 exceeds the XRT field of view and its high brightness largely dominates over the background even at the boundary. However, since the computation of three-dimensional profiles at the radius r needs to account for the emission at larger radii $r' > r$, and those are not available when outside the field of view, radii close to the boundaries are biased and we restricted the analysis to $r < 500\,\mathrm{kpc}$ for *Swift*. In the *XMM-Newton* dataset for A2029 there are additional pointings covering the emission at large radii, and therefore the profiles are reliable out to larger radii. CL2015 is less affected by this problem because it has a smaller angular (sky) dimension than Abell 2029.

Broadly speaking, the three-dimensional thermodynamic profiles are derived using similar methods by us and Ghirardini et al. (2019) using both spatial and spectral data, but the details are different. Our treatment of the background is simpler because a more complex treatment is unnecessary for the stable and low XRT background (except at special locations, such as at low Galactic latitudes). Ghirardini et al. (2019) assume no temperature gradients in the derivation of the electron density profile and during the Abel inversion the number of photons in the annuli is computed from the median-averaged profile, while it is given by the mean-average profile (times the shell area) because regions of higher emissivity are not removed in their spectral analysis. Especially at the center, where the emitting volume is small and embedded in bright cluster emission, the XCOP choice underestimates the contamination of the outer shells.

In spite of these differences, profiles from different telescopes, analyses, and authors are within 10% (Fig. B.1). This indicates that (telescope, analysis, and authors) systematics are well below the 10% level and that our derivation of thermodynamic profiles is sophisticated enough compared to other state-of-the-art analyses. Our physical fit to *Swift* data gives $\log M(< 0.5\,\mathrm{Mpc})/M_\odot = 14.36 \pm 0.02$ vs. 14.44 ± 0.005 quoted in Ettori et al. (2019) from their XMM analysis, where errors are purely formal because deviations from the hydrostatic equilibrium hypothesis alone are at least on the order of $0.05-0.1$ dex, as quoted in Ettori et al. (2019).